Editors' Suggestion

# Interspecies interactions in an ultracold dipolar mixture

C. Politi,[1,2] A. Trautmann,[1,*] P. Ilzhöfer,[1,2,†] G. Durastante,[1,2] M. J. Mark,[1,2] M. Modugno,[3,4] and F. Ferlaino[1,2,‡]

[1]*Institut für Quantenoptik und Quanteninformation, Österreichische Akademie der Wissenschaften, 6020 Innsbruck, Austria*

[2]*Institut für Experimentalphysik, Universität Innsbruck, 6020 Innsbruck, Austria*

[3]*Department of Physics, University of the Basque Country UPV/EHU, 48080 Bilbao, Spain*

[4]*IKERBASQUE, Basque Foundation for Science, 48013 Bilbao, Spain*

(Received 19 October 2021; accepted 10 January 2022; published 3 February 2022)

We experimentally and theoretically investigate the influence of the dipole-dipole interactions (DDIs) on the total interspecies interaction in an erbium-dysprosium mixture. By rotating the dipole orientation we are able to tune the effect of the long-range and anisotropic DDI, and therefore the in-trap displacements of the erbium and dysprosium clouds. We present a theoretical description for our binary system based on an extended Gross-Pitaevskii theory, including the single-species beyond mean-field terms, and we predict a lower and an upper bound for the interspecies scattering length $a_{12} = 105[-65, +162]a_0$. Our work is a step towards the investigation of the experimentally unexplored dipolar miscibility-immiscibility phase diagram and the realization of quantum droplets and supersolid states with heteronuclear dipolar mixtures.

DOI: 10.1103/PhysRevA.105.023304

## I. INTRODUCTION

The ability to tune the interparticle interactions, the geometry and dimensionality of the system, and the possibility of adding complexity in a controlled manner, has made ultracold atomic gases a great platform for studying a plethora of physical phenomena that would be otherwise hard to achieve [1]. Combining two atomic species gives even further opportunities for investigating the effects arising from the interplay between the intra- and interspecies interactions, as polarons [2,3], heteronuclear quantum droplets [4–6], solitons [7], and ultracold molecules [8].

Heteronuclear mixtures are typically realized by combining contact-interacting atomic species (see alkali-alkali mixtures [9–15], alkali-alkaline-earth mixtures [16], and alkali-alkaline-earth-like mixtures [17–19]). Recently, experiments were able to produce novel types of ultracold mixtures where either one or both mixture components are long-range interacting (lanthanide) atomic species [20,21]. In particular, the realization of Er-Dy dipolar quantum mixtures is attracting great interest, driven by the possibility of creating new quantum phases even more exotic than the one achieved in contact-interacting mixtures [1] or in single-species dipolar gases [22]. Several theoretical works reported on the study of miscibility in dipolar condensates [23–26], vortex lattice formation [27,28], and on binary quantum droplets realized with dipolar mixtures [29–31].

In heteronuclear dipolar Bose-Bose mixtures, the phenomena mentioned above rely quite strongly on the miscibility-immiscibility conditions. These conditions define whether the two components mix together with the center of masses overlapping at the trap center or whether they are in a phase-separated state where the two centers of mass are pushed away from each other. The miscibility-immiscibility phase diagram depends on the contact intraspecies scattering lengths $a_{11}$, $a_{22}$ and dipolar lengths $a_{\mathrm{dd},1}$, $a_{\mathrm{dd},2}$, and the interspecies scattering lengths $a_{12}$ and dipolar lengths $a_{\mathrm{dd},12}$. While $a_{\mathrm{dd},12}$ can be calculated analytically, $a_{12}$ is unknown and its determination relies on experimental measurements.

In this paper, we prepare ultracold degenerate mixtures of erbium and dysprosium, and experimentally investigate the effect of the mean-field dipole-dipole interactions on the total interspecies interaction by tracing the center-of-mass displacement for different dipole orientations. We present a theoretical description for our system, including the single-species beyond mean-field terms, which reproduces qualitatively well the experiment. By matching theory and experiment, we define a lower and upper bound for the interspecies scattering length $a_{12}$.

## II. THEORY

Here, we consider a binary mixture of dipolar condensates of $^{164}$Dy and $^{166}$Er atoms confined in a harmonic potential, in the presence of a magnetic field $\boldsymbol{B}$ aligned along an arbitrary direction in space. The system can be described in terms of an extended Gross-Pitaevskii energy functional $E = E_{\mathrm{MF}} + E_{\mathrm{dd}} + E_{\mathrm{LHY}}$ with.

$$E_{\mathrm{MF}} = \sum_{i=1}^{2} \int \left[ \frac{\hbar^2}{2m_i} |\nabla \psi_i(\boldsymbol{r})|^2 + V_i(\boldsymbol{r}) |\psi_i(\boldsymbol{r})|^2 \right] d\boldsymbol{r} + \sum_{i,j=1}^{2} \frac{g_{ij}}{2} \int n_i(\boldsymbol{r}) n_j(\boldsymbol{r}) d\boldsymbol{r}, \quad (1)$$

$$E_{\mathrm{dd}} = \sum_{i,j=1}^{2} \frac{C_{ij}^{\mathrm{dd}}}{2} \iint n_i(\boldsymbol{r}) V_{\mathrm{dd}}(\boldsymbol{r} - \boldsymbol{r}') n_j(\boldsymbol{r}') d\boldsymbol{r} d\boldsymbol{r}', \quad (2)$$

*Present address: Physikalisches Institut, Auf der Morgenstelle 14 (D-Bau), 72076 Tübingen, Germany.

†Present address: 5. Physikalisches Institut and Center for Integrated Quantum Science and Technology, Universität Stuttgart, Pfaffenwaldring 57, 70569 Stuttgart, Germany.

‡Corresponding author: francesca.ferlaino@uibk.ac.at

 

and the single-species Lee-Huang-Yang (LHY) correction for the two components

$$E_{\rm LHY} = \frac{256\sqrt{\pi}}{15}\sum_{i=1}^{2}\frac{\hbar^2 a_{ii}^{5/2}}{m_i}\left(1+\frac{3}{2}\epsilon_{{\rm dd},i}^2\right)\int n_i(\boldsymbol{r})^{5/2}d\boldsymbol{r}, \quad (3)$$

where $n_i(\boldsymbol{r}) = |\psi_i(\boldsymbol{r})|^2$ represents the density of each condensate, $V_i(\boldsymbol{r}) = (m_i/2)\sum_{\alpha=x,y,z}\omega_{\alpha,i}^2 r_\alpha^2 + m_i g z$ includes the harmonic trapping and gravity potentials, $g_{ij} = 2\pi\hbar^2 a_{ij}(m_i + m_j)/(m_i m_j)$ is the contact interaction strength, $V_{\rm dd}(\boldsymbol{r}) = (1 - 3\cos^2\bar{\theta})/(4\pi r^3)$ the (bare) dipole-dipole potential, $C_{ij}^{\rm dd} \equiv \mu_0 d_i d_j$ its strength, $d_i$ the modulus of the dipole moment $\boldsymbol{d}_i$ of each species, $\epsilon_{{\rm dd},i} = \mu_0 d_i^2/3g_{ii}$ [32], $\boldsymbol{r}$ the distance between the dipoles, and $\bar{\theta}$ the angle between the vector $\boldsymbol{r}$ and the dipole axis, $\cos\bar{\theta} = \boldsymbol{d}\cdot\boldsymbol{r}/(dr)$ [33]. In the following we identify species 1 with the Er condensate, and species 2 with the Dy condensate (we have also omitted the reference to the mass number, for ease of notations). As described later on, the orientation of the magnetic dipoles is varied along arbitrary directions through an external magnetic field $\boldsymbol{B}$.

Then, for each set of parameters the ground state of the system is obtained by minimizing the energy functional $E[\psi_1, \psi_2]$ by means of a conjugate algorithm (see, e.g., Refs. [33–35]). In the numerical code the double integral appearing in Eq. (2) is mapped into Fourier space where it can be conveniently computed using fast Fourier transform (FFT) algorithms, after regularization (see Appendix B). The LHY correction in Eq. (3) is obtained from the expression for homogeneous three-dimensional (3D) dipolar condensates under the local-density approximation [32,36]. For the sake of simplicity, here we do not include the interspecies LHY correction as it would require a much more complicated treatment [29,30], which is not essential when the system is stable against the mean-field collapse driven by the interspecies interactions, as in the present analysis.

Finally, we remark that the intraspecies scattering lengths are given as the input to the theory and, whereas the value for Er has been measured with high accuracy to be $a_{11} = 83(3)a_0$ at the magnetic field we are working at [37], the scattering length for Dy, $a_{22}$, still lacks an accurate determination. Several works have reported different values ranging from $60a_0$ to $100a_0$ [38,39]. As in the present work no signs of supersolid or droplet states have been observed [40], we set $a_{22}$ to the minimal value for which Dy is stable against mean-field collapse (without LHY), namely $a_{22} = 95a_0$. This guarantees that the ground state is an unmodulated BEC, for our atom numbers and trap frequencies. Note that, since $a_{11} > a_{{\rm dd},1}$ while $a_{22} \leqslant a_{{\rm dd},2}$, with $a_{{\rm dd},i} = C_{ii}^{\rm dd} m_i/(12\pi\hbar^2)$ the dipolar length, we expect Eq. (3) to be more relevant for Dy than for Er. Indeed, when dropping this term for Er, we observe no changes in the behavior. Instead, for Dy, the system would collapse for $a_{22} < 95a_0$ for $\boldsymbol{B}$ perpendicular to the gravity direction.

## III. EXPERIMENT

Our experiment starts with a degenerate mixture of $^{166}$Er and $^{164}$Dy, similar to Ref. [21]. In brief, after cooling the atomic clouds in a dual-species magneto-optical trap [41], we start the evaporative cooling by loading the mixture into a single-beam optical dipole trap at 1064 nm, which propagates horizontally ($y$ axis); see the reference frame in Fig. 1(a). After about 600 ms, the power of a second trapping beam, propagating vertically along the direction of gravity ($z$ axis), is linearly ramped up to form a crossed optical dipole trap (cODT). Here, the evaporation further proceeds for about 5 s. We perform the evaporation at a magnetic field of $B = 2.028$ G, pointing along the $z$ axis, which allows an efficient cooling of both species.

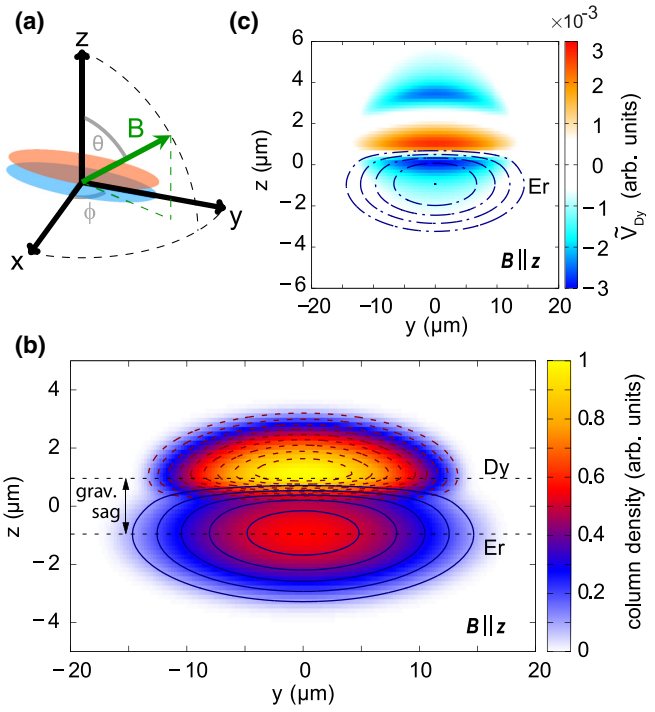


FIG. 1. Trap geometry, ground-state column density, and dipole potential. (a) Illustration of the geometry of our $^{164}$Dy (red ellipse) and $^{166}$Er (blue ellipse) mixture. The orientation of the magnetic field is defined by the angles $\phi$ and $\theta$. The imaging beam propagates in the horizontal plane, at an angle of 45° with respect to the $y$ axis (not shown). (b) Ground-state column density for an imbalanced mixture with $N_{\rm Dy} = 1.3\times10^4$, $N_{\rm Er} = 4.9\times10^4$, $a_{12} = 100a_0$. Dashed and solid lines show the isodensity contour levels for Dy and Er, respectively. For comparison, the in-trap displacement due to the gravitational sag for a noninteracting mixture is also shown (black dashed lines). We set $z = 0$ at the center of the gravitational sag. (c) Heat map of the dipole potential produced by the Dy condensate (parameters below), $\tilde{V}_{Dy}(\boldsymbol{r}) \equiv \int V_{\rm dd}(\boldsymbol{r}-\boldsymbol{r}')n_{Dy}(\boldsymbol{r}')d\boldsymbol{r}'$, in the $x = 0$ plane. Here, the magnetic field points along the $z$ axis. The dotted-dashed lines represent the isodensity contour levels of the Er component, indicating that in this regime the interspecies dipolar interaction is predominantly attractive.

The final harmonic trap has a cigarlike shape, axially elongated along the $y$ axis, with frequencies $\omega_{x,y,z} = 2\pi\times[96(1), 18(1), 150(5)]$ s$^{-1}$, and $\omega_{x,y,z} = 2\pi\times[104(1), 18(1), 165(5)]$ s$^{-1}$ for Er and Dy, respectively. The trapping frequencies of the two species slightly differ. This is due to the small difference in their mass and atomic polarizability [42,43]. In a harmonic trap, each species experiences a shift of its center-of-mass (COM) position along the $z$ axis due to gravity. This effect is known as

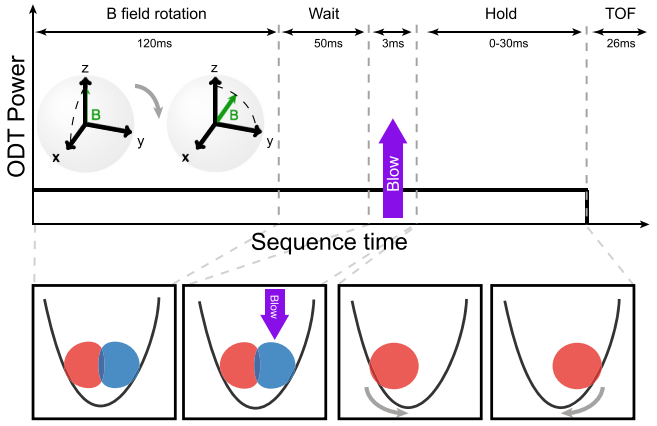


FIG. 2. Experimental protocol. After preparing our Er-Dy mixture with $\boldsymbol{B} \parallel z$, the magnetic field is rotated to an arbitrary direction, defined by $\theta$ and $\phi$, in 120 ms. The atomic clouds are held in the trap for 50 ms to reach equilibrium, before either of the species is removed with resonant light. The remaining cloud is held for a variable hold time $t_h$. The cloud is then released from the trap and imaged with standard absorption imaging after a TOF expansion of $t_{\mathrm{TOF}} = 26$ ms. We prepare imbalanced mixtures with condensed atom numbers $N_{\mathrm{C}}$ in the range $[1\text{–}3] \times 10^4$ and $[4\text{–}6] \times 10^4$ for Dy and Er, respectively (see Appendix A).

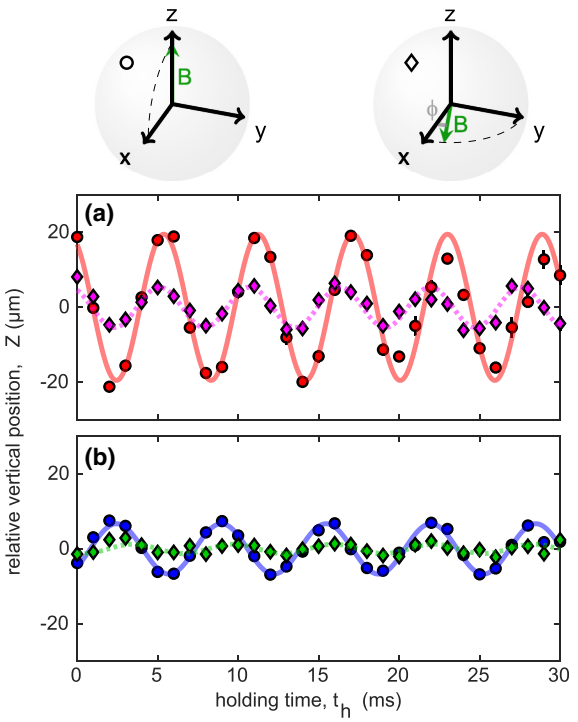


FIG. 3. COM oscillations after removal of either one of the species. (a) Vertical COM position of Dy after removing Er and (b) vice versa. The vertical position $Z_i$ is recorded after a TOF expansion of 26 ms, as a function of the holding time. The offset $z_{\mathrm{off}}$ has been subtracted to facilitate comparison. The measurements are repeated for two magnetic-field orientations: $\boldsymbol{B} \parallel z$, $\theta = 0°$, $\phi = 0°$ (circles) and $\boldsymbol{B} \in \boldsymbol{xy}$, $\theta = 90°$, $\phi = 15°$ (diamonds). The atom numbers are $N_{\mathrm{Dy}} = 1.3(2) \times 10^4$, $N_{\mathrm{Er}} = 4.9(7) \times 10^4$ and $N_{\mathrm{Dy}} = 3.1(5) \times 10^4$, $N_{\mathrm{Er}} = 4.7(5) \times 10^4$ for $\boldsymbol{B} \parallel z$ and $\boldsymbol{B} \in \boldsymbol{xy}$, respectively. The error bars reported represent the standard error on the mean over three experimental trials, and are mostly smaller than the markers. We fit Eq. (4) to the data for $\boldsymbol{B} \parallel z$ (solid lines) and $\boldsymbol{B} \in \boldsymbol{xy}$ (dotted lines).

gravitational sag [44–46]. For mixtures, the differential gravitational sag between the components is given by $\Delta z_{\mathrm{grav}} = g(1/\omega_{z1}^2 - 1/\omega_{z2}^2)$, which for our Er-Dy mixture is $\Delta z_{\mathrm{grav}} = 1.9(1)\ \mu$m with Er shifted downwards more than Dy; see Fig. 1(a). Such gravitational sag favors phase separation along the $z$ axis, reducing the interspecies overlap density. In the presence of interspecies interactions, the vertical distance of the clouds' centers is not only determined by the gravitational sag but also by their mutual mean-field attraction or repulsion [13,15,47–49], quantified by the mean-field shift $\Delta z_{\mathrm{MF}}$. For dipolar mixtures, $\Delta z_{\mathrm{MF}}$ is determined by the interplay between the dipolar and contact interspecies interactions, as we will discuss later. The total vertical in-trap displacement is thus $\Delta z = \Delta z_{\mathrm{grav}} + \Delta z_{\mathrm{MF}}$.

Figure 1(b) shows exemplary calculations of the 2D ground-state column density of an imbalanced mixture for $\boldsymbol{B} \parallel z$ and $a_{12} = 100 a_0$. In this configuration, a COM shift is clearly visible, which exceeds the gravitational sag, indicating a total repulsive mean-field interaction between the components. To understand the role of the DDI, it is interesting to calculate the effective potential generated by one species (e.g., Dy), $\widetilde{V}_{Dy}(\boldsymbol{r}) \equiv \int V_{\mathrm{dd}}(\boldsymbol{r} - \boldsymbol{r}') n_{Dy}(\boldsymbol{r}') d\boldsymbol{r}'$, felt by the other species (e.g., Er). Such effective potentials are most relevant in the region where the two species overlap (beside a long-range tail from the DDI). As shown in Fig. 1(c), for our trap geometry and dipole orientation, Er experiences a dominant attractive DDI generated by Dy, which is however weaker than the repulsive interspecies contact interaction for $a_{12} = 100 a_0$.

To experimentally study the interspecies mean-field shift, we selectively remove either one of the two species and follow the COM dynamics of the remaining species towards its new equilibrium position in the trap [21]. Figure 2 illustrates our protocol. After preparing our trapped Bose-Bose Er-Dy mixture with $\boldsymbol{B} \parallel z$, we first adiabatically rotate the magnetic field in 120 ms to the desired orientation (i.e., changing $\theta$ and $\phi$) and let the mixture equilibrate for 50 ms. We then selectively remove either Er or Dy by shining a resonant light pulse, operating on either of the two strong atomic transitions [401 nm (421 nm) for Er (Dy)]. We have checked that this resonant pulse of 3-ms duration does not affect the remaining species. Finally, we hold the remaining species in trap for a variable time $t_h$ and probe the system with standard absorption imaging after a time-of-flight (TOF) expansion of $t_{\mathrm{TOF}} = 26$ ms.

After the selective removal of either of the two species, the remaining species is out of equilibrium and the cloud COM starts to oscillate around its new equilibrium position, given by the dipole-trap minimum in the presence of gravity. Figure 3(a) [Fig. 3(b)] shows the vertical COM position $Z_i$ (see Appendix A), measured after TOF, for Dy (Er) after removing Er (Dy) and for two different dipole orientations.

The amplitude of the observed oscillation is directly connected to the interspecies mean-field shift experienced by the atoms in the trap. Within the assumption of ballistic expansion, which is justified in the weakly interact-

ing regime, $Z_i(t_h, t_{\rm TOF}) = z_i(t_h) + \dot{z}_i(t_h)t_{\rm TOF} + gt_{\rm TOF}^2/2$, where $z_i(t_h) = \Delta z_{{\rm MF},i}\cos(\omega_i t_h) + \Delta z_{\rm grav}$ is the in-trap COM position. The oscillation frequency $\omega_i$ is the trap frequency along the $z$ axis.

By combining the previous equations, one gets the following expression,

$$Z_i(t_h, t_{\rm TOF}) = \Delta z_{{\rm MF},i}\cos(\omega_i t_h) - \Delta z_{{\rm MF},i}\,\omega_i \sin(\omega_i t_h)t_{\rm TOF} + z_{\rm off}, \tag{4}$$

where $z_{\rm off} = \Delta z_{\rm grav} + gt_{\rm TOF}^2/2$. We fit Eq. (4) to the experimental data for the two magnetic-field orientations with the mean-field shift $\Delta z_{{\rm MF},i}$, $\omega_i$, and $z_{\rm off}$ being free fitting parameters.

## IV. RESULTS

Figure 3 shows important information on the interspecies interactions. First, by comparing the dynamics of the two species, we observe that the oscillations are counterphase. The Dy cloud starts moving downwards towards the trap center, whereas the Er one moves upwards, confirming a total repulsive interspecies interaction for this geometry. Second, we see a clear difference in the oscillation amplitude between Dy and Er. This is due to the fact that the mixture is imbalanced with Er being the majority species, and therefore the mean-field shift caused by Er on Dy is larger. Finally, for each species, the oscillation amplitude strongly depends on the magnetic-field orientation. This behavior cannot be simply explained by the anisotropy of the DDI. For $\boldsymbol{B} \parallel z$, the DDI is more attractive over the interspecies overlap region than for $\boldsymbol{B}$ in the $xy$ plane, $\boldsymbol{B} \in \boldsymbol{xy}$. Hence, one would expect $\Delta z_{\rm MF,z} < \Delta z_{\rm MF,xy}$, contrasting the observations.

The additional effect to account for is the magnetostriction [50] of each species, i.e., a cloud elongation along the magnetization direction caused by the single-species DDI. For $\boldsymbol{B} \parallel \boldsymbol{z}$, the two clouds elongate along the $z$ axis, thus increasing the interspecies overlap density; see Fig. 1(b). This increased overlap activates a backaction on the strength of the repulsive contact interaction, which acquires a larger weight, leading to an increased repulsion between the clouds. On the contrary, for $\boldsymbol{B} \in \boldsymbol{xy}$, the clouds elongate horizontally, thereby minimizing the overlap density and therefore the interspecies repulsion. The slight difference in frequency observed for the two magnetic-field orientations is due to the presence of small residual magnetic-field gradients (see Appendix C).

To get further insight into the anisotropy of the interspecies interactions, we repeat the above measurement for various dipole orientations, set by the angles $\theta$ and $\phi$. As before, we perform two sets of measurements: We probe the out-of-equilibrium dynamics of Dy after removing Er and vice versa. To enhance the amplitude of the COM oscillations of one species (Dy), we perform measurements with imbalanced mixtures, where Er is the majority species with condensed atom numbers in the range $[4\text{–}6] \times 10^4$, while the Dy cloud contains about $[1\text{–}3] \times 10^4$ (see Appendix A).

Figure 4 summarizes our results. It shows both the measured and calculated mean-field shift $\Delta z_{{\rm MF},i}$ for each plane of rotation for Dy (red points) and Er (blue points). We observe that $\Delta z_{{\rm MF},i}$ has a maximum for $\boldsymbol{B} \parallel \boldsymbol{z}$ and decreases when approaching the horizontal plane. The gray lines show the theory

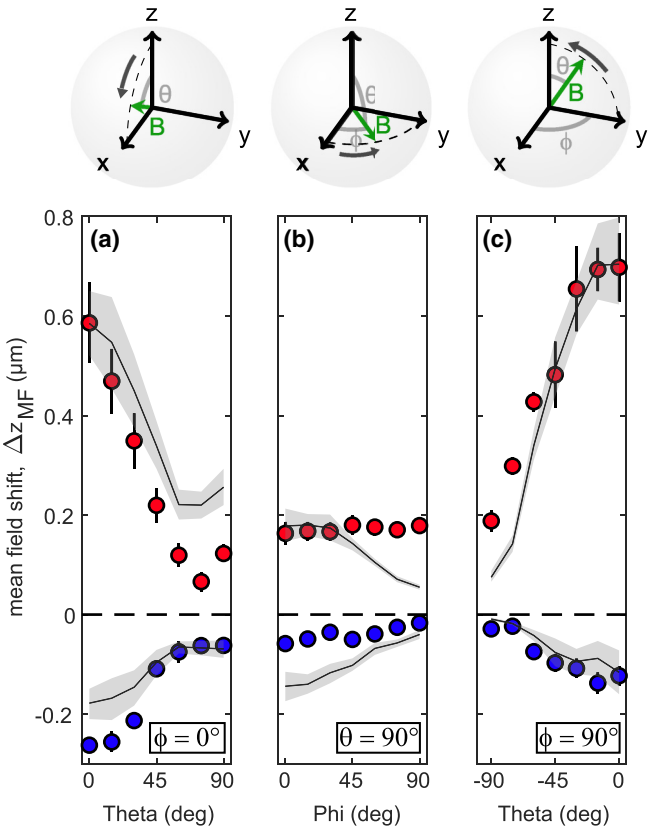


FIG. 4. Mean-field displacement and theory prediction. Experimental estimation of the mean-field displacement $\Delta z_{{\rm MF},i}$ for Dy (red points) and Er (blue points), as a function of the magnetic-field orientation. (a) $\theta = [0°, 90°]$, $\phi = 0°$. (b) $\phi = [0°, 90°]$, $\theta = 90°$. (c) $\theta = [0°, 90°]$, $\phi = 90°$. Theory prediction for an interspecies scattering length $a_{12} = 100a_0$ (gray lines). The gray shaded area takes into account the experimental uncertainty on the estimation of the atom number. The error bars in $\Delta z_{{\rm MF},i}$ correspond to the statistical uncertainty from the fit. The mismatch between the data points at $\theta = 0°$ in (a) and (c) is due to different atom numbers (see Appendix A).

results for an interspecies scattering length $a_{12} = 100a_0$ and for our experimental parameters, i.e., atom numbers and trap frequencies. We chose $a_{12} = 100a_0$ as it describes best the experimental data. The gray shaded area takes into account the experimental uncertainty on the estimation of the atom number.

The theory curves agree qualitatively with the experimental observations. In particular, experiment and theory are in good agreement for $\boldsymbol{B} \parallel \boldsymbol{z}$, while they start to deviate for $\boldsymbol{B} \in \boldsymbol{xy}$. The small mismatch can be due to the presence of residual vertical magnetic-field gradients, which are not taken into account in the theory. These can cause a systematic shift of the trap frequencies to higher values when going from $\boldsymbol{B} \parallel \boldsymbol{z}$ to $\boldsymbol{B} \in \boldsymbol{xy}$, thereby reducing the gravitational sag (see Appendix C). Furthermore, while our Dy ground-state calculations predict the transition to a macrodroplet at $a_{22} = 95a_0$ for $\boldsymbol{B} \parallel \boldsymbol{y}$, and a further reduction of the overlap density, in the experiment we observe a stable Dy BEC. Previous works have also shown a quantitative mismatch between theory and

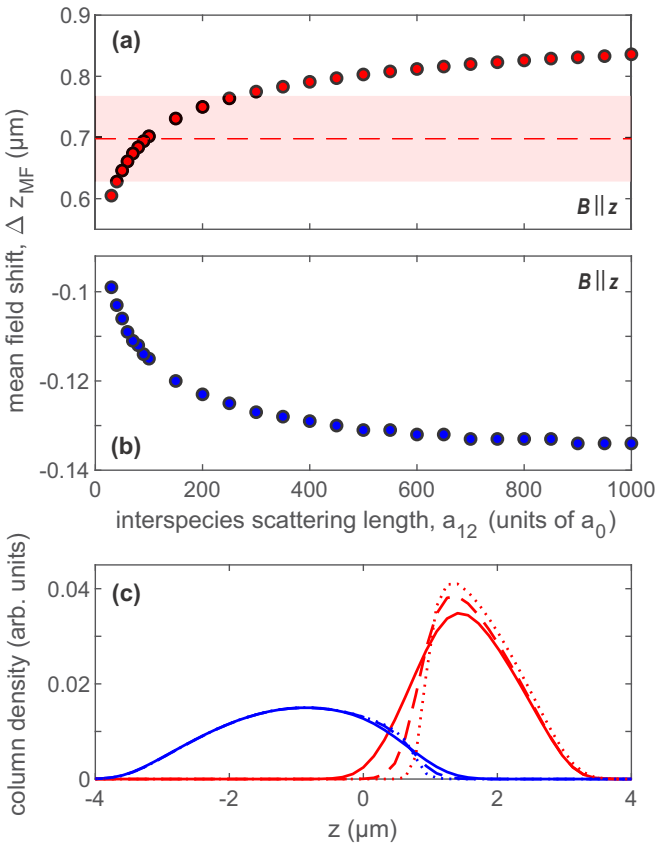


FIG. 5. Calculated mean-field displacement as a function of $a_{12}$. Calculated mean-field displacement for (a) Dy and (b) Er as a function of the interspecies scattering length $a_{12}$. The red dashed line and the red shaded area in (a) represent the Dy experimental mean-field displacement and its error, respectively. The magnetic field is oriented along the $z$ axis. (c) In-trap density cut along $y = 0$ for Dy (red) and Er (blue), for $a_{12} = 30a_0$ (solid lines), $a_{12} = 100a_0$ (dashed lines), and $a_{12} = 200a_0$ (dotted lines). Here, $N_{\mathrm{Dy}} = 0.8 \times 10^4$ and $N_{\mathrm{Er}} = 5.9 \times 10^4$.

experiment in predicting the macrodroplet transition, suggesting the need for refined models and an accurate determination of $a_{22}$ [36,37,51].

The overall behavior shown in Fig. 4 can be explained by the effect of the magnetostriction on the interspecies overlap density. In fact, as discussed earlier, for magnetic-field orientations in the horizontal plane, the clouds are elongated horizontally along the direction of $\boldsymbol{B}$, thereby minimizing the density overlap and the interspecies repulsion, whereas when orienting the magnetic field along the vertical direction, the magnetostriction leads to an increase of the density overlap and therefore of the interspecies repulsion, which overcomes the attractive DDI. The system undergoes a transition to a state where the two components are pushed aside, maximizing the in-trap displacement [see Fig. 1(b)].

To study the behavior of the mean-field shift as a function of $a_{12}$, we consider a specific magnetic-field orientation. In particular, for $\boldsymbol{B} \parallel \boldsymbol{z}$, we perform ground-state calculations varying the interspecies scattering length $a_{12}$ and calculate the Er-Dy mean-field displacement as a function of $a_{12}$. The results are shown in Fig. 5. The mean-field displacement increases with $a_{12}$ owing to the fact that Dy [Fig. 5(a)] is pushed away from Er [Fig. 5(b)]. Figure 5(c) shows the Dy (red) and Er (blue) density cuts along $y = 0$, for $a_{12} = 30a_0$ (solid lines), $a_{12} = 100a_0$ (dashed lines), and $a_{12} = 200a_0$ (dotted lines). The repulsive interaction between the species leads to a decrease of the density overlap when going to higher $a_{12}$. We compare the theory results with the experimentally measured mean-field shift at $[\theta = 0°, \phi = 90°]$, and by performing a $\chi^2$ analysis we are able to estimate the interspecies scattering length to be $a_{12} = 105[-65, +162]a_0$ (see Appendix D). From our ground-state calculations, when choosing $a_{12} < 30a_0$ the repulsive contribution of the contact interactions to the mean-field shift is not enough to overcome the attractive contribution from the DDI [see Fig. 1(c)] leading to a collapse of both species. In this regime, it might be necessary to include the interspecies LHY term as done in Refs. [29,30].

## V. CONCLUSIONS AND OUTLOOK

In conclusion, we have experimentally investigated the effect of the DDI on the total interspecies interaction by tracing the mean-field in-trap displacement between the species. We have presented a theoretical description for our Er-Dy mixture, including the single-species beyond mean-field corrections, which qualitatively describes well our system and allows us to predict an interspecies scattering length on the order of $a_{12} = 100a_0$. By changing the magnetic-field orientation from the horizontal plane to the vertical direction, we were able to observe a transition to a state in which the two components are pushed apart by the dominant mean-field repulsive interaction. Future studies will focus on the use of interspecies Feshbach resonances, recently reported in our group [52], to reach the conditions in which one or both components exhibit a phase transition to a quantum droplet or supersolid regime. As an example, Fig. 6 shows that the onset of a supersolid phase in the Dy component can be induced by increasing the interspecies contact scattering length $a_{12}$.

## ACKNOWLEDGMENTS

We thank Maximilian Sohmen for experimental support and for valuable discussions. We thank Rick van Bijnen for theoretical support. We also thank Lauriane Chomaz, Matthew Norcia, Lauritz Klaus, and the Innsbruck Erbium team for fruitful discussions. This work is financially supported through an ERC Consolidator Grant (RARE, No. 681432), the QuantERA grant MAQS by the Austrian Science Fund FWF No. I4391-N, the DFG/FWF via FOR 2247/I 4317-N36, and the FWF Grant No. I4426 RSF/Russia 2019. M.M. acknowledges support through Grant No. PGC2018-101355-B-I00 funded by MCIN/AEI/10.13039/501100011033 and by ERDF A way of making Europe, and by the Basque Government through Grant No. IT986-16. We also acknowledge the Innsbruck Laser Core Facility, financed by the Austrian Federal Ministry of Science, Research and Economy.

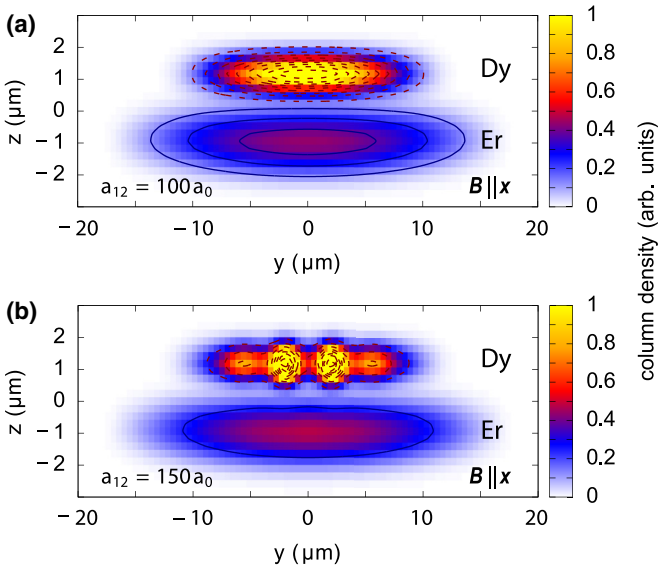


FIG. 6. Calculation of an interaction-induced supersolidity. Ground-state configurations for an imbalanced dipolar mixture with the magnetic field pointing along the $x$ axis, for two different values of the interspecies scattering length: (a) $a_{12} = 100a_0$, (b)$\boldsymbol{a_{12} = 150a_0}$. Dashed and solid lines show the isodensity contour levels for Dy and Er, respectively. Here, $N_{\mathrm{Dy}} = 1.2 \times 10^4$, $N_{\mathrm{Er}} = 6 \times 10^4$, $a_{11} = 83a_0$, and $a_{22} = 95a_0$.

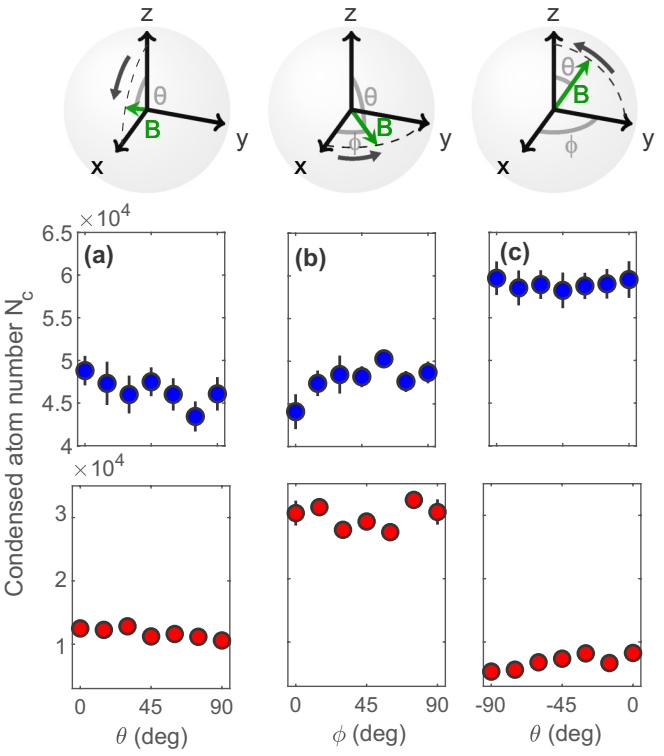


FIG. 7. Condensed atom numbers as a function of the magnetic-field orientation. Measured atom numbers in the BEC for Dy (red points) and Er (blue points) related to the measurement shown in Fig. 4 of the main text. The magnetic field is oriented (a) in the $XZ$ plane, (b) in the $XY$ plane, and (c) in the $YZ$ plane. The error bars reported represent the standard error on the mean over three experimental trials.

## APPENDIX A: ATOM NUMBER AND VERTICAL COM POSITION

After each experimental sequence—described in Fig. 2—we release the clouds and perform absorption imaging after a TOF expansion of 26 ms. We measure the condensed atom number for each species after subtracting the thermal part by fitting a symmetric 2D Gaussian to the wings of the density distribution. We then fit an asymmetric Gaussian to the remaining density distribution to extract the vertical COM position $Z_i$. Figure 7 shows the measured condensed atom numbers $N_{\mathrm{C}}$ of Dy (red points) and Er (blue points), related to the results presented in Fig. 4 of the main text. These atom numbers are given as input to the theory for each value of $\theta$ and $\phi$.

## APPENDIX B: FOURIER REPRESENTATION AND REGULARIZATION OF THE DIPOLAR ENERGY

Here, we outline the method used for calculating the double integral in Eq. (2), following the standard approach introduced in Ref. [33]. As anticipated, we start by rewriting the above integral in Fourier space. In particular, we make use of the *Parseval theorem* [34], $\int g(\boldsymbol{x})h^*(\boldsymbol{x})d\boldsymbol{x} = \int \tilde{g}(\boldsymbol{k})\tilde{h}^*(\boldsymbol{k})d\boldsymbol{k}$, where $\tilde{g}(\boldsymbol{k}) \equiv \mathrm{FT}[g](\boldsymbol{k})$ and $\tilde{h}^*(\boldsymbol{k}) \equiv \{\mathrm{FT}[h](\boldsymbol{k})\}^*$. Then, by defining $f \equiv h^*$ and recalling that $\mathrm{FT}[f^*](\boldsymbol{k}) = \tilde{f}^*(-\boldsymbol{k})$, we have $\tilde{h}^*(\boldsymbol{k}) = \{\mathrm{FT}[f^*](\boldsymbol{k})\}^* = \tilde{f}(-\boldsymbol{k})$, so that

$$E_{\mathrm{dd}} = \frac{1}{2}\int \tilde{n}_i^*(\boldsymbol{k})\widetilde{V}_{\mathrm{dd}}(\boldsymbol{k})\tilde{n}_j(\boldsymbol{k})d\boldsymbol{k}, \tag{B1}$$

where we have used the fact that $n_i(\boldsymbol{r})$ is real, which implies $\tilde{n}_i(-\boldsymbol{k}) = \tilde{n}_i^*(\boldsymbol{k})$ [53]. At this point it is worth recalling that the use of the FT implicitly entails a periodic system, and this brings along an unwanted effect: The long-range dipolar interactions can couple the system to virtual periodic replica. Such a coupling is obviously unphysical, and it can be cured by limiting the range of the dipolar interaction within a sphere of radius $R$ (contained inside the computational box of size $L$), namely multiplying $V_{\mathrm{dd}}(\boldsymbol{r})$ by the Heaviside step function $\Theta(R - r)$, with $R \leqslant L/2$. The corresponding FT is [33]

$$\widetilde{V}_{\mathrm{dd}}^{\mathrm{cut}}(\boldsymbol{k}) = 4\pi\left(1 + 3\frac{\cos(Rk)}{R^2k^2} - 3\frac{\sin(Rk)}{R^3k^3}\right)\left(\cos^2\alpha - \frac{1}{3}\right). \tag{B2}$$

## APPENDIX C: ESTIMATION OF THE RESIDUAL MAGNETIC-FIELD GRADIENT

To evaluate the residual magnetic-field gradient we measure the COM position of Er and Dy as a function of the TOF and for different values of the magnetic field. In this way, we are able to extract the correction to the gravitational acceleration $g$ due to residual magnetic-field gradients. When $\boldsymbol{B}$ is oriented along the $z$ axis we measure an increase in $g$ of about 2% for Dy and 1% for Er. The presence of these residual magnetic-field gradients along the direction of gravity leads to a slight decrease of the trap frequencies (see Fig. 3 in the main text) when orienting $\boldsymbol{B}$ from the $XY$ plane to the $z$ axis. The tensorial polarizability [42,54] could also cause a shift

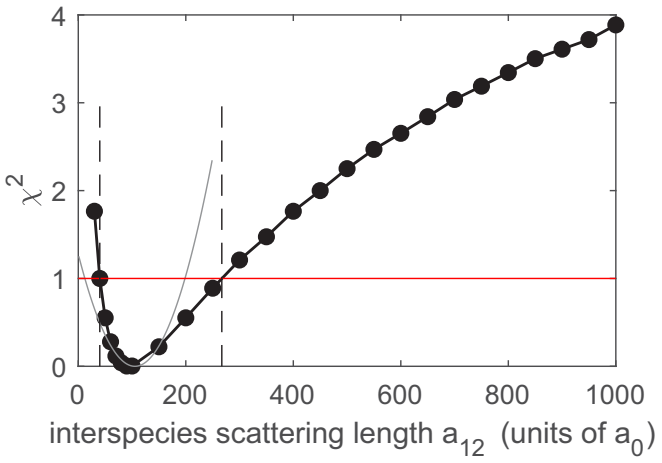


FIG. 8. $\chi^2$ distribution of the mean-field shift. $\chi^2$ distribution for the Dy mean-field shift (black points). We estimate the interspecies scattering length to be $a_{12} = 105[-65, +162]a_0$, by locally doing a Gaussian fit around the minimum of the distribution (gray line) and by defining the lower and upper bounds as the values at which $\chi^2 = 1$ (black dashed lines).

of the trap frequencies when changing the orientation of the magnetic field, but these are negligible in our case.

## APPENDIX D: ESTIMATION OF THE INTERSPECIES SCATTERING LENGTH

From the calculated mean-field shift as a function of the interspecies scattering length, shown in Fig. 5 of the main text, we can estimate the value of $a_{12}$ that best represents the experimental results and its confidence interval. Since Er is the majority species, its mean-field displacement is less sensitive to the change in interspecies scattering length [as shown in Fig. 5(b)]. In particular, the change in mean-field shift is within the experimental error. Therefore, we only take Dy into account for our analysis. We perform a $\chi^2$ analysis for the Dy mean-field shift at $[\theta = 0°, \phi = 90°]$, with $\chi^2 = (\Delta z_{\mathrm{MF},2} - \Delta z^{\mathrm{th}}_{\mathrm{MF},2})^2/\sigma^2_{\Delta z_{\mathrm{MF},2}}$, where $\Delta z^{\mathrm{th}}_{\mathrm{MF},2}$ is the theoretically calculated in-trap mean-field displacement, and $\Delta z_{\mathrm{MF},2}$ and $\sigma_{\Delta z_{\mathrm{MF},2}}$ the experimental value and its statistical error. By fitting a Gaussian around the minimum of the distribution and by defining its confidence interval as the range in which $\chi^2 < 1$ [55], we estimate $a_{12} = 105[-65, +162]a_0$, see Fig. 8.


[1] I. Bloch, J. Dalibard, and W. Zwerger, Many-body physics with ultracold gases, Rev. Mod. Phys. **80**, 885 (2008).

[2] M.-G. Hu, M. J. Van de Graaff, D. Kedar, J. P. Corson, E. A. Cornell, and D. S. Jin, Bose Polarons in the Strongly Interacting Regime, Phys. Rev. Lett. **117**, 055301 (2016).

[3] N. B. Jørgensen, L. Wacker, K. T. Skalmstang, M. M. Parish, J. Levinsen, R. S. Christensen, G. M. Bruun, and J. J. Arlt, Observation of Attractive and Repulsive Polarons in a Bose-Einstein Condensate, Phys. Rev. Lett. **117**, 055302 (2016).

[4] D. S. Petrov, Quantum Mechanical Stabilization of a Collapsing Bose-Bose Mixture, Phys. Rev. Lett. **115**, 155302 (2015).

[5] C. R. Cabrera, L. Tanzi, J. Sanz, B. Naylor, P. Thomas, P. Cheiney, and L. Tarruell, Quantum liquid droplets in a mixture of Bose-Einstein condensates, Science **359**, 301 (2018).

[6] C. D'Errico, A. Burchianti, M. Prevedelli, L. Salasnich, F. Ancilotto, M. Modugno, F. Minardi, and C. Fort, Observation of quantum droplets in a heteronuclear bosonic mixture, Phys. Rev. Research **1**, 033155 (2019).

[7] B. J. DeSalvo, K. Patel, G. Cai, and C. Chin, Observation of fermion-mediated interactions between bosonic atoms, Nature (London) **568**, 61 (2019).

[8] K.-K. Ni, S. Ospelkaus, M. H. G. de Miranda, A. Pe'er, B. Neyenhuis, J. J. Zirbel, S. Kotochigova, P. S. Julienne, D. S. Jin, and J. Ye, A high phase-space-density gas of polar molecules, Science **322**, 231 (2008).

[9] G. Modugno, G. Ferrari, G. Roati, R. J. Brecha, A. Simoni, and M. Inguscio, Bose-Einstein condensation of potassium atoms by sympathetic cooling, Science **294**, 1320 (2001).

[10] Z. Hadzibabic, C. A. Stan, K. Dieckmann, S. Gupta, M. W. Zwierlein, A. Görlitz, and W. Ketterle, Two-Species Mixture of Quantum Degenerate Bose and Fermi Gases, Phys. Rev. Lett. **88**, 160401 (2002).

[11] M. Mudrich, S. Kraft, K. Singer, R. Grimm, A. Mosk, and M. Weidemüller, Sympathetic Cooling with Two Atomic Species in an Optical Trap, Phys. Rev. Lett. **88**, 253001 (2002).

[12] C. Silber, S. Günther, C. Marzok, B. Deh, P. W. Courteille, and C. Zimmermann, Quantum-Degenerate Mixture of Fermionic Lithium and Bosonic Rubidium Gases, Phys. Rev. Lett. **95**, 170408 (2005).

[13] D. J. McCarron, H. W. Cho, D. L. Jenkin, M. P. Köppinger, and S. L. Cornish, Dual-species Bose-Einstein condensate of $^{87}$Rb and $^{133}$Cs, Phys. Rev. A **84**, 011603(R) (2011).

[14] J. W. Park, C.-H. Wu, I. Santiago, T. G. Tiecke, S. Will, P. Ahmadi, and M. W. Zwierlein, Quantum degenerate Bose-Fermi mixture of chemically different atomic species with widely tunable interactions, Phys. Rev. A **85**, 051602(R) (2012).

[15] L. Wacker, N. B. Jørgensen, D. Birkmose, R. Horchani, W. Ertmer, C. Klempt, N. Winter, J. Sherson, and J. J. Arlt, Tunable dual-species Bose-Einstein condensates of $^{39}$K and $^{87}$Rb, Phys. Rev. A **92**, 053602 (2015).

[16] B. Pasquiou, A. Bayerle, S. M. Tzanova, S. Stellmer, J. Szczepkowski, M. Parigger, R. Grimm, and F. Schreck, Quantum degenerate mixtures of strontium and rubidium atoms, Phys. Rev. A **88**, 023601 (2013).

[17] A. Khramov, A. Hansen, W. Dowd, R. J. Roy, C. Makrides, A. Petrov, S. Kotochigova, and S. Gupta, Ultracold Heteronuclear Mixture of Ground and Excited State Atoms, Phys. Rev. Lett. **112**, 033201 (2014).

[18] V. D. Vaidya, J. Tiamsuphat, S. L. Rolston, and J. V. Porto, Degenerate Bose-Fermi mixtures of rubidium and ytterbium, Phys. Rev. A **92**, 043604 (2015).

[19] K. E. Wilson, A. Guttridge, J. Segal, and S. L. Cornish, Quantum degenerate mixtures of Cs and Yb, Phys. Rev. A **103**, 033306 (2021).

[20] C. Ravensbergen, V. Corre, E. Soave, M. Kreyer, E. Kirilov, and R. Grimm, Production of a degenerate Fermi-Fermi mixture of dysprosium and potassium atoms, Phys. Rev. A **98**, 063624 (2018).

[21] A. Trautmann, P. Ilzhöfer, G. Durastante, C. Politi, M. Sohmen, M. J. Mark, and F. Ferlaino, Dipolar Quantum Mixtures of Erbium and Dysprosium Atoms, Phys. Rev. Lett. **121**, 213601 (2018).

[22] M. A. Norcia and F. Ferlaino, Developments in atomic control using ultracold magnetic lanthanides, Nat. Phys. **17**, 1349 (2021).

[23] R. M. Wilson, C. Ticknor, J. L. Bohn, and E. Timmermans, Roton immiscibility in a two-component dipolar Bose gas, Phys. Rev. A **86**, 033606 (2012).

[24] R. K. Kumar, P. Muruganandam, L. Tomio, and A. Gammal, Miscibility in coupled dipolar and non-dipolar Bose–Einstein condensates, J. Phys. Commun. **1**, 035012 (2017).

[25] K.-T. Xi, T. Byrnes, and H. Saito, Fingering instabilities and pattern formation in a two-component dipolar Bose-Einstein condensate, Phys. Rev. A **97**, 023625 (2018).

[26] R. K. Kumar, L. Tomio, and A. Gammal, Spatial separation of rotating binary Bose-Einstein condensates by tuning the dipolar interactions, Phys. Rev. A **99**, 043606 (2019).

[27] R. K. Kumar, L. Tomio, B. A. Malomed, and A. Gammal, Vortex lattices in binary Bose-Einstein condensates with dipole-dipole interactions, Phys. Rev. A **96**, 063624 (2017).

[28] R. K. Kumar, L. Tomio, and A. Gammal, Vortex patterns in rotating dipolar Bose–Einstein condensate mixtures with squared optical lattices, J. Phys. B: At., Mol. Opt. Phys. **52**, 025302 (2018).

[29] R. N. Bisset, L. A. Pena Ardila, and L. Santos, Quantum Droplets of Dipolar Mixtures, Phys. Rev. Lett. **126**, 025301 (2021).

[30] J. C. Smith, D. Baillie, and P. B. Blakie, Quantum Droplet States of a Binary Magnetic Gas, Phys. Rev. Lett. **126**, 025302 (2021).

[31] J. C. Smith, P. B. Blakie, and D. Baillie, Approximate theories for binary magnetic quantum droplets, Phys. Rev. A **104**, 053316 (2021).

[32] F. Wächtler and L. Santos, Ground-state properties and elementary excitations of quantum droplets in dipolar Bose-Einstein condensates, Phys. Rev. A **94**, 043618 (2016).

[33] S. Ronen, D. C. E. Bortolotti, and J. L. Bohn, Bogoliubov modes of a dipolar condensate in a cylindrical trap, Phys. Rev. A **74**, 013623 (2006).

[34] W. H. Press, S. A. Teukolsky, W. T. Vetterling, and B. P. Flannery, *Numerical Recipes: The Art of Scientific Computing*, 3rd ed. (Cambridge University Press, New York, 2007).

[35] M. Modugno, L. Pricoupenko, and Y. Castin, Bose-Einstein condensates with a bent vortex in rotating traps, Eur. Phys. J. D **22**, 235 (2003).

[36] M. Schmitt, M. Wenzel, F. Böttcher, I. Ferrier-Barbut, and T. Pfau, Self-bound droplets of a dilute magnetic quantum liquid, Nature (London) **539**, 259 (2016).

[37] L. Chomaz, S. Baier, D. Petter, M. J. Mark, F. Wächtler, L. Santos, and F. Ferlaino, Quantum-Fluctuation-Driven Crossover from a Dilute Bose-Einstein Condensate to a Macrodroplet in a Dipolar Quantum Fluid, Phys. Rev. X **6**, 041039 (2016).

[38] Y. Tang, A. Sykes, N. Q. Burdick, J. L. Bohn, and B. L. Lev, *s*-wave scattering lengths of the strongly dipolar bosons $^{162}$Dy and $^{164}$Dy, Phys. Rev. A **92**, 022703 (2015).

[39] I. Ferrier-Barbut, M. Wenzel, F. Böttcher, T. Langen, M. Isoard, S. Stringari, and T. Pfau, Scissors Mode of Dipolar Quantum Droplets of Dysprosium Atoms, Phys. Rev. Lett. **120**, 160402 (2018).

[40] L. Chomaz, D. Petter, P. Ilzhöfer, G. Natale, A. Trautmann, C. Politi, G. Durastante, R. M. W. van Bijnen, A. Patscheider, M. Sohmen, M. J. Mark, and F. Ferlaino, Long-Lived and Transient Supersolid Behaviors in Dipolar Quantum Gases, Phys. Rev. X **9**, 021012 (2019).

[41] P. Ilzhöfer, G. Durastante, A. Patscheider, A. Trautmann, M. J. Mark, and F. Ferlaino, Two-species five-beam magneto-optical trap for erbium and dysprosium, Phys. Rev. A **97**, 023633 (2018).

[42] J. H. Becher, S. Baier, K. Aikawa, M. Lepers, J.-F. Wyart, O. Dulieu, and F. Ferlaino, Anisotropic polarizability of erbium atoms, Phys. Rev. A **97**, 012509 (2018).

[43] C. Ravensbergen, V. Corre, E. Soave, M. Kreyer, S. Tzanova, E. Kirilov, and R. Grimm, Accurate Determination of the Dynamical Polarizability of Dysprosium, Phys. Rev. Lett. **120**, 223001 (2018).

[44] M. Modugno, F. Ferlaino, F. Riboli, G. Roati, G. Modugno, and M. Inguscio, Mean-field analysis of the stability of a K-Rb Fermi-Bose mixture, Phys. Rev. A **68**, 043626 (2003).

[45] A. H. Hansen, A. Y. Khramov, W. H. Dowd, A. O. Jamison, B. Plotkin-Swing, R. J. Roy, and S. Gupta, Production of quantum-degenerate mixtures of ytterbium and lithium with controllable interspecies overlap, Phys. Rev. A **87**, 013615 (2013).

[46] F. Wang, X. Li, D. Xiong, and D. Wang, A double species $^{23}$Na and $^{87}$Rb Bose–Einstein condensate with tunable miscibility via an interspecies Feshbach resonance, J. Phys. B: At., Mol. Opt. Phys. **49**, 015302 (2015).

[47] S. B. Papp, J. M. Pino, and C. E. Wieman, Tunable Miscibility in a Dual-Species Bose-Einstein Condensate, Phys. Rev. Lett. **101**, 040402 (2008).

[48] K. L. Lee, N. B. Jørgensen, I.-K. Liu, L. Wacker, J. J. Arlt, and N. P. Proukakis, Phase separation and dynamics of two-component Bose-Einstein condensates, Phys. Rev. A **94**, 013602 (2016).

[49] K. E. Wilson, A. Guttridge, I.-K. Liu, J. Segal, T. P. Billam, N. G. Parker, N. P. Proukakis, and S. L. Cornish, Dynamics of a degenerate Cs-Yb mixture with attractive interspecies interactions, Phys. Rev. Research **3**, 033096 (2021).

[50] J. Stuhler, A. Griesmaier, T. Koch, M. Fattori, T. Pfau, S. Giovanazzi, P. Pedri, and L. Santos, Observation of Dipole-Dipole Interaction in a Degenerate Quantum Gas, Phys. Rev. Lett. **95**, 150406 (2005).

[51] F. Böttcher, M. Wenzel, J.-N. Schmidt, M. Guo, T. Langen, I. Ferrier-Barbut, T. Pfau, R. Bombín, J. Sánchez-Baena, J. Boronat, and F. Mazzanti, Dilute dipolar quantum droplets beyond the extended Gross-Pitaevskii equation, Phys. Rev. Research **1**, 033088 (2019).

[52] G. Durastante, C. Politi, M. Sohmen, P. Ilzhöfer, M. J. Mark, M. A. Norcia, and F. Ferlaino, Feshbach resonances in an erbium-dysprosium dipolar mixture, Phys. Rev. A **102**, 033330 (2020).

[53] We notice that the expression in Eq. (A8) of Ref. [33] can be used only if $n(\boldsymbol{r})$ is even under parity in the three spatial directions, namely when $\tilde{n}(-\boldsymbol{k}) = \tilde{n}(\boldsymbol{k})$.

[54] H. Li, J.-F. Wyart, O. Dulieu, and M. Lepers, Anisotropic optical trapping as a manifestation of the complex electronic structure of ultracold lanthanide atoms: The example of holmium, Phys. Rev. A **95**, 062508 (2017).

[55] P. Young, *Everything You Wanted to Know About Data Analysis and Fitting but Were Afraid to Ask* (Springer, Berlin, 2015).